ROYAL SOCIETY
OF CHEMISTRY

PAPER

Low-cost silicon cutting waste reused as a high-power-density silicon-based anode

Lanxiang Huang, [ID] †*[abc] Jialin Wang,†[c] Yu Hu,[abc] Chang Chen,[c] Liujun Cao [ID] *[d] and Qiang Jiang*[b]

With the rapid development of electric vehicle technology, commercial graphite anodes (theoretical capacity of 372 mA h g^{-1}) of lithium-ion batteries cannot meet the needs for high power density. Silicon has high theoretical capacity (4200 mA h g^{-1}), low working voltage (about 0.4 V *vs.* Li/Li$^+$), rich resources and environmental friendly nature; hence, it is regarded as a potential negative electrode material. During repeated charging and discharging, silicon particles continuously pulverize, which leads to the volume expansion of electrode materials (up to 400%) and a decrease in conductivity. In this study, high-purity nano-silicon was prepared *via* a calcination-ball milling-pickling process with low-cost silicon cutting waste (SiCW) as a raw material to meet the needs of lithium-ion batteries for high-purity and nano-scale silicon-based anodes. At the same time, silicon@graphite nanocomposites with different mass ratios were prepared *via* a low-cost industrialized ball-milling process. The easy intercalation and softness of the graphite layer structure realized the coating and joining of nano-silicon, which improved the conductivity of nano-silicon and restrained the rapid degradation of cycling performance caused by the expansion and pulverization of the silicon-based anode. Adopting low-cost raw materials and industrialization-based preparation processes can effectively control the production cost of silicon-based anode materials and lay a solid foundation for their practicality.

1. Introduction

Lithium-ion batteries are widely used in portable consumer electronics and exhibit huge potential in areas such as electric vehicles and grid-based energy storage.[1] With the rapid development of electric vehicle technology, the demand for high-energy-density, high-power-density, long-life and high-safety lithium-ion batteries has increased dramatically, making the development of new lithium-ion battery materials with high capacity, high stability and low cost a current research focus.[2,3] Commercial graphite has low specific capacity (theoretical capacity of 372 mA h g^{-1}), which makes it difficult to use it as an anode material for high-energy-density lithium-ion batteries.[4,5] Among the known new anode materials, silicon has high theoretical capacity (4200 mA h g^{-1}), low working voltage (about 0.4 V *vs.* Li/Li$^+$), rich resources and environmentally friendly

nature, and it is therefore regarded as a potential negative electrode material.[6]

Li and Si can form alloy phases such as $Li_{12}Si_7$, Li_7Si_3, $Li_{13}Si_4$, and $Li_{22}Si_5$.[7] As the intercalation of lithium into silicon increases, when the internal stress of silicon particles is larger than the fracture strength of silicon particles, the cracking of silicon particles occurs. Because the intercalation of lithium begins on the surface of silicon particles and the Li–Si alloy phase on the surface of silicon particles is more brittle, cracks generally form on the surface, expand and increase in the subsequent repeated charging and discharging processes. As a result, silicon particles are continuously pulverized, which leads to the volume expansion of the electrode material (up to 400%) and a decrease in its conductivity.[8] Researchers found that the size of silicon particles depends on whether the silicon materials were pulverized or not during the process of lithium alloying. When the diameter of spherical silicon nanoparticles is less than 150 nm, the pulverization of nano-silicon materials can be alleviated.[9,10] Meanwhile, silicon is a semiconductor material, and its low intrinsic conductivity is also a problem that cannot be ignored compared with other anode materials such as graphite and tin [11,12]. Therefore, the introduction or coating of conductive materials (such as metal nanoparticles,[13–15] carbon-based materials,[16] and MXenes[17]) is widely used to solve the problems of silicon-based negative electrodes. However, the synthesis of these silicon-based

[a]Crystalline Silicon Photovoltaic New Energy Research, Leshan Normal University, Leshan, Sichuan, 614000, China. E-mail: 120678486@qq.com

[b]West Silicon Photovoltaic New Energy Industry Technology Research Institute, Leshan, Sichuan, 614000, China. E-mail: 23549504@qq.com

[c]School of New Energy Materials and Chemistry, Leshan Normal University, Leshan, Sichuan, 614000, China

[d]College of Materials and Chemistry & Chemical Engineering, Chengdu University of Technology, Chengdu, Sichuan, 610000, China. E-mail: caoliujun19@cdut.edu.cn

† These authors contributed equally to this work.

composites often involves complex processes, harsh reaction conditions, and high-cost raw materials,[18,19] and the cost of nanocrystalline silicon (about \$16 000-a-tonne silicon-based anode, \$4000-a-tonne graphite anode) has also greatly limited the practical application of silicon-based anode materials. Therefore, the development of low-cost, high-performance silicon-based anode materials for high-energy density lithium-ion batteries for practical applications is of great significance.

Global photovoltaic power generation with an annual growth rate of more than 35% resulted in a steady increase in silicon wafer production.[20] More than 40% of crystalline silicon becomes the cutting waste in the multi-wire cutting process of monocrystalline silicon rods.[21] At present, the cutting-waste silicon material in China has reached more than 200 000 tons, and is mainly used as metallurgical silicon after recycling;[22] the recovery price is \$690-a-tonne of dry powder. In this work, low-cost cutting-waste silicon was used as a raw material to prepare high-purity nano-silicon particles by pretreatment, and then compounded with graphite to improve the electrochemical performance of silicon anodes.

Graphite is a layered crystal structure of a hexagonal carbon network.[23] It is formed by combining carbon atoms in the form of a sp^2 hybrid. There is a van der Waals force between the layers, and hence, the binding force between the layers is much smaller than the binding force in the layers; therefore, some atoms, ions and groups are easily intercalated between the graphite layers to form intercalated compounds. Graphite has a complete crystal structure, which is stable and has a small volume expansion coefficient in the process of lithium ion disintercalation, and it is a good conductor with good ionic and electronic conductivity. Silicon materials can play the following roles by combining with graphite: first, it can buffer the volume expansion of silicon and help to maintain the stability of the whole electrode; second, it is advantageous to the even dispersion of silicon in carbon; third, it reduces the voltage lag of the composite; and fourth, the graphite itself can provide a stable reversible capacity of about 300 mA h g^{-1}.

2. Experimental

2.1 Preparation of Si@graphite composites

The silicon cutting waste (SiCW) used was provided by QING-DAO GAOCE Technology Co., Ltd (Leshan, China). The raw SiCW agglomerations were pre-treated before use due to a large amount of surfactants and metallic impurities. First, raw SiCW was calcined at 600 °C for 2 h in a tube furnace to decompose the organic surfactant with argon used as the protecting gas. After that, the SiCW was ground into a silicon cutting waste powder (SiCWP) and then washed with dilute HCl (1 M) for 2 h at room temperature to remove the metal impurities. Finally, the high-purity SiCWP was mixed with the commercial micron graphite by ball milling at mass ratios of 1/1, 4/6, 3/7, 2/8 and 1/9, and the Si/graphite composites were labeled $Si_{50}G_{50}$, $Si_{40}G_{60}$, $Si_{30}G_{70}$, $Si_{20}G_{80}$, and $Si_{10}G_{90}$, respectively.

2.2 Material characterization

The structure of materials was characterized by X-ray diffraction measurements (XRD, DX-2600X, Cu-Kα1). Thermogravimetric analysis (TG, NETZSCH 209F1) under air atmosphere was tested at a rate of 20 °C min^{-1} to determine the graphite content. Raman characterization was carried out to check the state of graphite by micro Raman spectroscopy (Renishaw inVia reflex) at an excitation wavelength of 532 nm under ambient conditions. The electronic conductivity of the Si/graphite composites was tested to identify the change in the electronic conductivity of silicon while administering graphite using an RTS-8 Four Probe Tester. The surface morphologies and microstructures of SiCW, SiCWP, Si/graphite composites, and electrodes before and after cycling were observed using a field emission scanning electron microscope (FE-SEM, thermo scientific Apreo 2C). The internal microstructure of $Si_{20}G_{80}$ composites was measured using a transmission electron microscope and a high-resolution transmission electron microscope (HRTEM, JEM2100). The concentration of impurities in SiCWP was determined by inductively coupled plasma-atomic emission spectroscopy (ICP-AES) method (PerkinElmer Avio 200).

2.3 Electrochemical test

The active substance, acetylene black and binder (carboxyl methyl cellulose) were mixed in deionized water in a mass ratio of 8 : 1 : 1 to form a homogeneous slurry, which was then uniformly spread onto a copper foil. After that the pasted foil was dried in a vacuum oven at 80 °C for 12 hours and then cut into discs of 12 mm diameter. The active substance was pure Si, graphite or Si/graphite composites, the average mass was about 1.6 mg and the capacity was calculated based on the mass of the active substance. The CR2032 coin-type half-cells were assembled in a glove box filled with argon. A lithium foil and a polyethylene film were used as the counter electrode and separator respectively. The electrolyte consists of 1 M LiPF$_6$ dissolved in ethylene carbonate (EC) and diethyl carbonate (DEC) (EC : DEC = 1 : 1 vol%) with 5% FEC. Although the theoretical specific capacity of silicon is very high, it decays sharply in the cycle process and the actual cycling specific capacity is low; therefore, the nominal specific capacity of silicon and Si/graphite composites was set as 400 mA h g^{-1}, for the pure graphite, and the value was 372 mA h g^{-1}. All cells were tested at a voltage in the range of 2.0–0.01 V (vs. Li/Li$^+$) using an electrochemical test system (LAND, CT3001A). The cyclic voltammetry curve (CV) and electrochemical impedance spectra (EIS) were measured using an electrochemical workstation (DongHua Analytical, DH7000).

3. Results and discussions

3.1 Morphology and structure

In the photovoltaic industry, SiCW is produced in the process of multi-wire diamond cutting of single-crystal silicon rods. More than 40% of crystalline silicon was cut into SiCW depending on the ratio between the diameter of the diamond wire and the thickness of the silicon wafer. Due to the shear force between

the diamond wire and the silicon substrate, the obtained SiCW had a lamellar structure[24] (Fig. 1a). After pre-treatment, the morphology of the SiCWP was characterized as a nanoparticle (Fig. 1b) by field emission scanning electron microscopy (FE-SEM). The types and contents of impurities were tested by ICP-OES analysis, and 21.1 ppmw B, 11.89 ppmw Ca, 11.3 ppmw Fe, 1.51 ppmw Mn and 242 ppmw Ni were found in the SiCWP; in other words, the purity of the SiCWP is as high as 99.9997% (Table 1).

Fig. 2a shows the XRD patterns of Si/graphite composites with different mass ratios. It can be seen that the Si/graphite composites have the characteristic diffraction peaks of Si and graphite, and the characteristic peak strength of Si decreases with the reduction in silicon content. The graphite contents of $Si_{50}G_{50}$, $Si_{40}G_{60}$, $Si_{30}G_{70}$, $Si_{20}G_{80}$, and $Si_{10}G_{90}$ samples were 50.02%, 60.82%, 70.05%, 79.52% and 89.63% (Fig. 2b), respectively, which is consistent with the experimental ratio. The Raman spectra of graphite and Si/graphite composites show two remarkable peaks at around 1338 and 1587 cm^{-1} (Fig. 2c) corresponding to the well-defined D band and G band, respectively. It is well known that the G band related to the E_{2g} vibration mode of sp^2 carbon domains can be used to explain the degree of graphitization, while the D band is associated with the structural defects and partially disordered structures of the sp^2 domains.[25] It clearly shows that the intensity of the G band is much higher than that of the D band in graphite; on the contrary, the intensity of the G band becomes weaker than that of the D band in Si/graphite composites, indicating much more defects in Si/graphite composites than that in graphite. The electronic conductivity of the Si/graphite composites was tested, and the results are presented in Table 2. Obviously, with the increase in the amount of graphite, the conductivity increases gradually.

Graphite exhibited a micron-scale flake structure (Fig. 3a). The morphology of Si/graphite composited with different mass ratios of SiCWP (Fig. 3b) is displayed as secondary particles formed by the aggregation of smaller nanoparticles (Fig. 3c–g), and no flake graphite was seen. There are three possibilities for the disappearance of flake graphite: first, it is coated onto the surface of nano-silicon particles during ball milling; second, it

Table 1 Impurity content and purity of SiCWP

Impurity elements	B	Ca	Fe	Mn	Ni	Purity (%)
Concentration (mg kg^{-1})	21.1	11.8	11.3	1.51	242	99.9997

is milled into nano-graphite particles; and third, nano-silicon particles are tightly attached onto the surface of flake graphite; thus, from the appearance, it looks like the secondary particles were formed by the agglomeration of nano-silicon particles. For this purpose, the $Si_{20}G_{80}$ composite was examined by TEM and HRTEM, as shown in Fig. 3g–i. The content of graphite in the $Si_{20}G_{80}$ composite is as high as 80%, but there is no large flake graphite; part acts as a bridge between the nano-silicon particles, connecting all the silicon particles as a whole. Spherical silicon nanoparticles (diameter less than 150 nm) can reduce the particle pulverization caused by repeated intercalation/delithiation during cycling, and the graphite coating on the silicon surface can buffer the volume change of silicon and restrain the volume expansion effectively. The uniform dispersion of nano-silicon in graphite carbon will effectively improve the electrical conductivity of silicon and ultimately improve the electrochemical performance of the silicon-based anode.

3.2 Electrochemical performance

The CV curves of six anode electrode materials after recycling three times are presented in Fig. 4a. For the Si/graphite composites, two reduction peaks (R_1, R_2) appeared between 0.16 and 0.19 V and 0 and 0.13 V, corresponding to the formation of lithium silicide (Li$_x$Si), and two oxidation peaks (O$_1$ and O$_2$) between 0.33 and 0.35 V and 0.51 and 0.53 V represented the release of Si from Li$_x$Si.[26,27] The peak current decreases with the increase in graphite content, because the specific capacity of graphite is lower than that of silicon. At the same time, with the increase in graphite content, the peak potential of R_1 and R_2 shifted to the right, and the peak potential of O$_1$ and O$_2$ shifted to the left, which means better reversibility as graphite increased. Obviously, the peak current of pure silicon is the
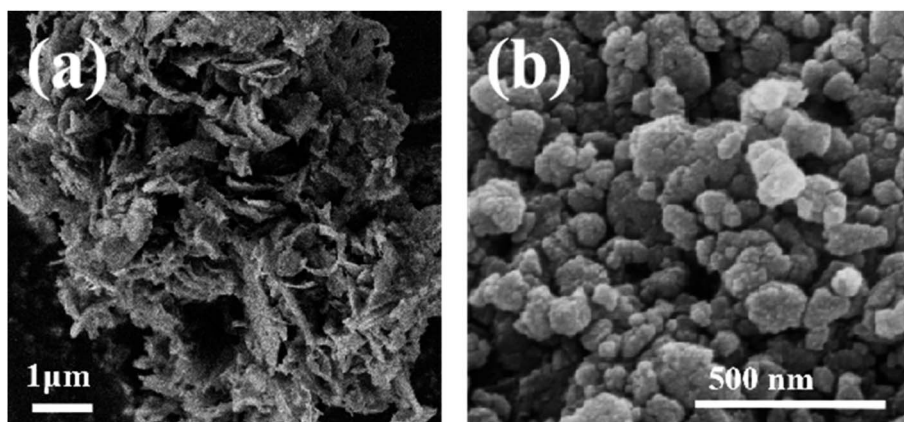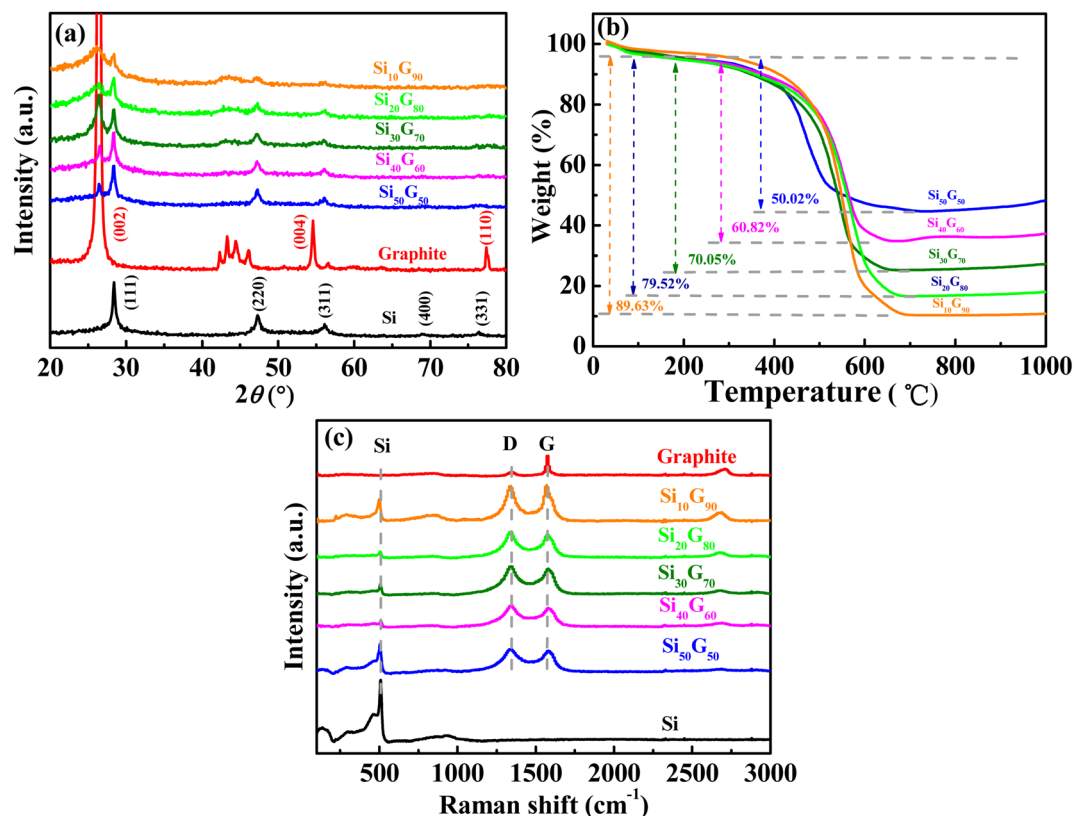

Fig. 1 Morphology of SiCW (a) and SiCWP (b).

Fig. 2 (a) XRD spectra, (b) TG curves, and (c) Raman spectrum of Si/graphite composites with different mass ratios.

lowest of all the curves, indicating that after only three cycles, pure silicon caused a sharp decline in capacity due to problems such as silicon particle volume expansion. Meanwhile, the most positive peak potential of oxidation peak and the most negative peak potential of reduction peak mean the worst cycle reversibility. Therefore, it can be concluded that although the composite of graphite materials reduces the specific capacity of silicon materials, most of them can improve the reversibility of materials, that is, cycling stability. Thus, the selection of graphite content needs to balance between the two according to the actual demand.

The electrochemical impedance spectroscopy (EIS) of graphite, Si, $Si_{50}G_{50}$, $Si_{40}G_{60}$, $Si_{30}G_{70}$, $Si_{20}G_{80}$ and $Si_{10}G_{90}$ semicells was performed at 100 kHz to 0.1 Hz, as shown in Fig. 4b, and the corresponding equivalent circuit is given in the inset picture. The semicircle in the high-frequency region is related to the charge transfer resistance (R_{CT}), and the straight line in the low-frequency region is related to the diffusion of lithium ions.[28] The R_{CT} value of Si is 115 Ω, and that of $Si_{50}G_{50}$, $Si_{40}G_{60}$, $Si_{30}G_{70}$, $Si_{20}G_{80}$, and $Si_{10}G_{90}$ decreases gradually as the graphite mass ratio increased, which is 86, 82, 69, 62, 55 Ω, respectively.

Of course, due to the excellent conductivity of graphite, it showed the lowest resistance (47 Ω). The trend is consistent with the conductivity test results (Table 2). The excellent conductivity of graphite can effectively enhance the electrical contact between the particles of active materials and reduce their charge transfer impedance.

The rate performance between 0.3 C and 2 C is shown in Fig. 4c. Because of the low theoretical specific capacity, graphite exhibits the lowest rate specific capacity. As to Si, due to the higher theoretical specific capacity, its specific capacity at 0.3 C is not low, but that decreases sharply when the rate increases to 0.5 C, which is much lower than that of Si/graphite composites. It can be seen that the $Si_{20}G_{80}$ composite has no capacity advantage at low rates (0.3 C), but it exhibits the highest discharge specific capacity as the rate increased to 1 C or even 2 C. Meanwhile, when returned to 0.3 C, $Si_{20}G_{80}$ still has the highest specific capacity. All the results indicate that $Si_{20}G_{80}$ has excellent fast charge–discharge performance, and good reversibility, very suitable for electric vehicles for fast charge requirements.

Table 2 Conductivity of different samples

Sample	Si	$Si_{50}G_{50}$	$Si_{40}G_{60}$	$Si_{30}G_{70}$	$Si_{20}G_{80}$	$Si_{10}G_{90}$	Graphite
Conductivity (mS cm^{-1})	7.4×10^{-3}	9.7×10^{2}	1.0×10^{3}	2.3×10^{3}	4.2×10^{3}	5×10^{3}	5×10^{5}
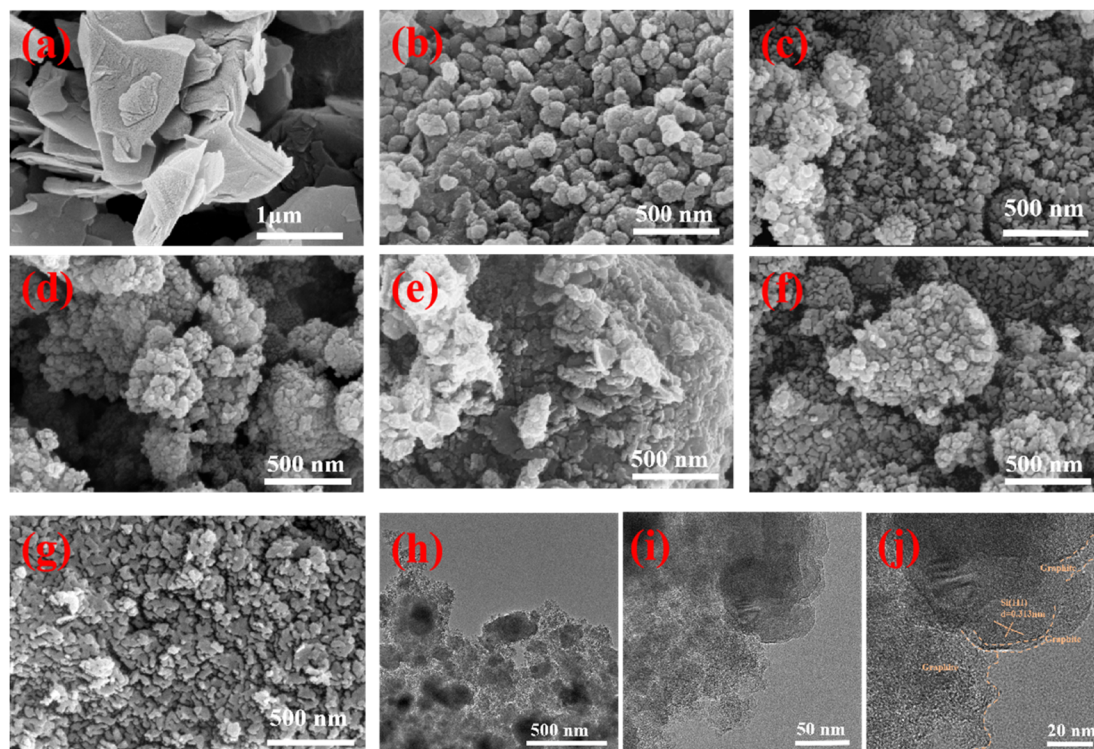
Fig. 3 SEM morphology of (a) graphite, (b) Si, (c) $Si_{50}G_{50}$, (d) $Si_{40}G_{60}$, (e) $Si_{30}G_{70}$, (f) $Si_{20}G_{80}$, and (g) $Si_{10}G_{90}$. TEM (h and i) and HRTEM (j) images of $Si_{20}G_{80}$ composites.

The cycling performance and stability were further investigated, as shown in Fig. 4d. Graphite had good cycling stability but low specific capacity, only 370 mA h g^{-1}, which is consistent with the theoretical specific capacity; however, this gradually decayed after 220 cycles, which may be ascribed to the large sheet of graphite that causes severe fragmentation and forms large cracks on the graphite electrode, thus leading to the disconnection of the active material from the current collector, which will be further studied later. The initial charge–discharge capacity of the pure silicon anode is very high, but it declined rapidly with cycling, and after 35 cycles, its specific capacity has been lower than graphite. It is well known that the intercalation of lithium into Si leads to severe volume expansion (up to 400%) in the repeated charging and discharging process, sharply weakens electrical contact between the active material and the current collector, and thus, deteriorated its cycling performance dramatically. As for $Si_{20}G_{80}$, although its initial charge–discharge capacity is 933.1 mA h g^{-1} only, it exhibits the most stable cycling performance. After 250 long cycles, the specific capacity is still as high as 316.7 mA h g^{-1}, and now that of graphite is 79.9 mA h g^{-1} only. In Si/graphite composites, silicon mainly takes advantage of its high specific capacity to increase the capacity of anode materials, while graphite mainly inhibits the volume expansion of silicon and improves its conductivity, thereby improving the cycling stability of the material. Therefore, with the increase in the graphite content, the initial capacity decreases, but the cycling performance is gradually improved. Obviously, as the proportion of graphite

continued to increase to 90%, the specific capacity of the composite was close to that of graphite, and the silicon's decay feature results in the capacity were lower than that of the graphite after 78 cycles. The charge/discharge profiles of 10th, 35th, 110th and 250th cycles in Fig. 4d are presented in Fig. 4e–h respectively.

To further elucidate the Li$^+$ electrochemical storage behavior, the CV curves of the $Si_{20}G_{80}$ electrode were tested at different scan rates and shown in Fig. 5a. It can be seen that the peak redox currents increased as the scan rate increased, indicating the rapid chemical kinetics of the $Si_{20}G_{80}$ electrode. The reduction–oxidation potential also shifted to negative and positive directions respectively, indicating that the reversibility decreased as the charge–discharge current density increased. In CV curves, the relationship between the peak current (i) and scan rate (v) can be described as $i = av^b$,[29,30] where b represents the slope of fitted curve $\log(i)$–$\log(v)$; when b is 0.5, it means a diffusion controlled behavior, and when b is 1.0, it means a surface reaction controlled process. As shown in Fig. 5b, the fitted curve $\log(i)$–$\log(v)$ presents a good linear relationship and the calculated slope b is 0.87, indicating that the chemical kinetics of the $Si_{20}G_{80}$ electrode is controlled by both diffusion and surface reaction controlled. In addition, according to the formula $i = k_1v + k_2v^{1/2}$, the capacitive contribution can be calculated.[31,32] At a fixed voltage of 0.5 V, different scan rates (v) correspond to different response currents (i). From the rearranged expression $i/v^{1/2} = k_1v^{1/2} + k_2$, k_1 and k_2 can be determined by the slope and intercept from the fitted curve $i/v^{1/2}$–$v^{1/2}$,
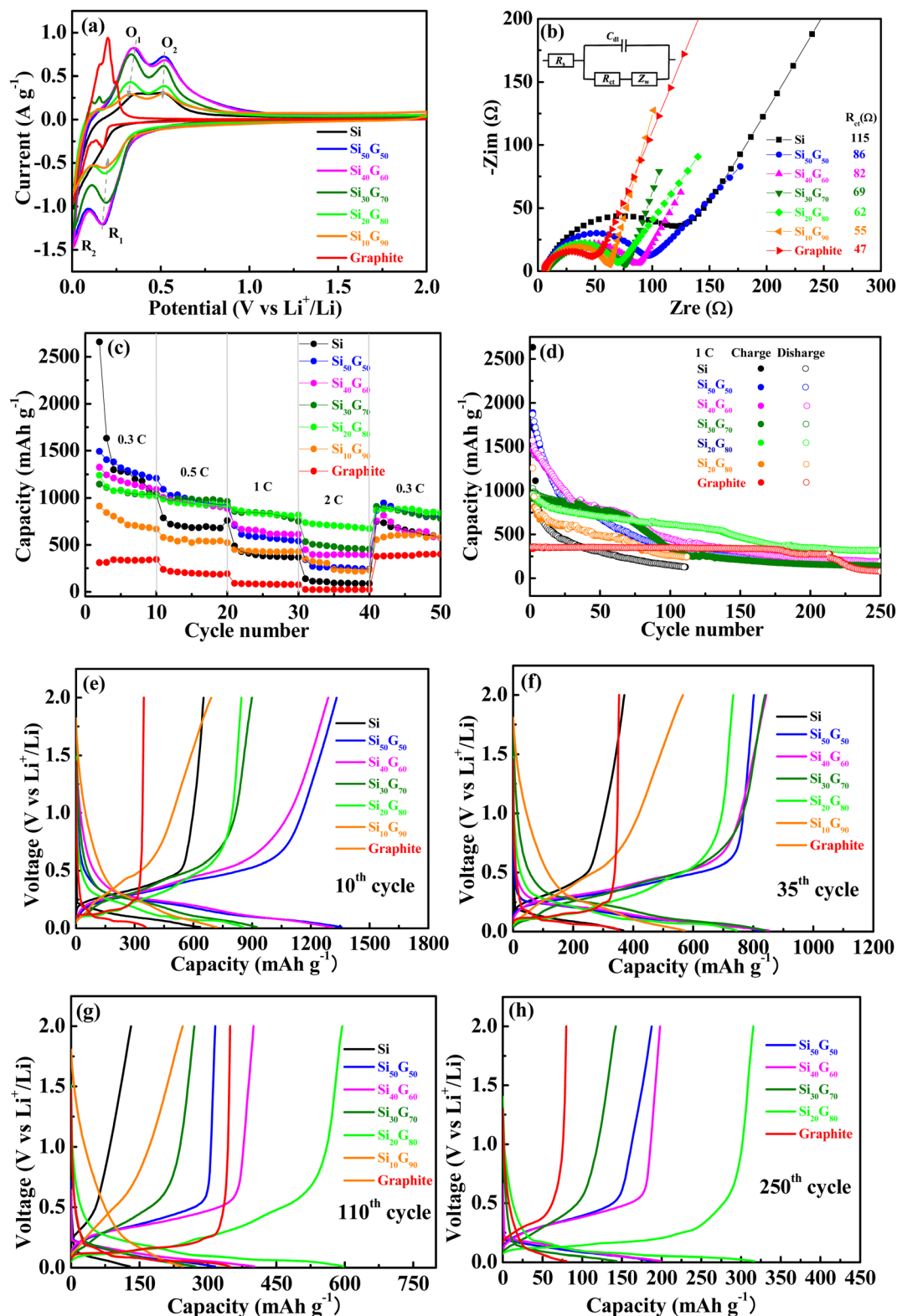
Fig. 4 (a) Cyclic voltammetry (CV), (b) electrochemical impedance spectroscopy (EIS), (c) rate performance, and (d) cycling performance curves at 1 C for all electrodes, with the charge/discharge profiles of (e) 10th, (f) 35th, (g) 110th and (h) 250th cycles in (d).

thus the values of $k_1\nu$ and $k_2\nu^{1/2}$ can be obtained, which correspond to the current contributions from the surface capacitive effects and the diffusion-controlled intercalation process,

respectively. The result of the calculation is shown in Fig. 5c. It can be seen that diffusion and capacitive effects affect the intercalation/extraction process of lithium ions, but the main
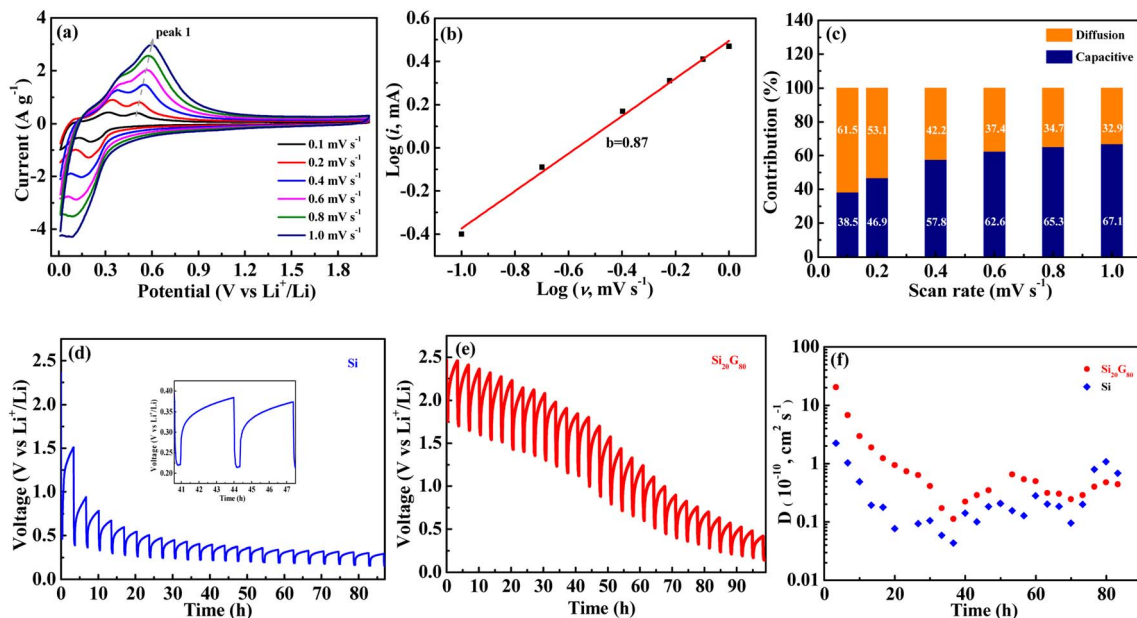
Fig. 5 (a) Cyclic voltammetry curves (CV), (b) log(i)/log(v) plots, and (c) capacitance and diffusion-controlled contributions at different scan rates of $Si_{20}G_{80}$ electrodes. GITT curves of (d) Si and (e) $Si_{20}G_{80}$ at the discharge state and (f) corresponding diffusion coefficients.

effect is contributed by diffusion behavior. With an increase in scanning rate, the effect of capacitive storage increased.

The diffusion kinetics was analyzed by the constant-current intermittent titration (GITT) technology. The cell was first discharged at 0.15 C for 20 minutes and then rested for 3 hours to reach the equilibrium state; the GITT curves of Si and $Si_{20}G_{80}$ are presented in Fig. 5d and e. The formula for calculating the diffusion coefficient (D) is as follows:[33]

$$D_{Zn^{2+}} = \frac{4}{\pi}\left(\frac{n_M V_M}{S}\right)^2 \left[\frac{\Delta E_s}{\tau(dE_\tau/d\sqrt{\tau})}\right]^2 \quad (\tau \ll L^2/D_{Zn^{2+}}) \quad (1)$$

where n_M, V_M, S, τ, ΔE_s, ΔE_τ and L represent the mole number (mol), mole volume ($cm^3\ mol^{-1}$) of active substances, the contact area of the electrode/electrolyte (cm^{-2}), discharge time (20 min), the changes in the steady-state voltage, the overall battery voltage after the current pulse applied in a single cycle (excluding IR voltage drop), and the thickness of the electrode, respectively. Obviously, the corresponding D value of $Si_{20}G_{80}$ is higher than that of Si (Fig. 5 f). The coating and connecting of graphite to silicon nanoparticles promote the diffusion kinetic performance of lithium ions.

The morphology evolution of graphite, Si and $Si_{20}G_{80}$ electrodes before and after cycling was further studied, as shown in Fig. 6. As can be seen, all the electrodes are quite flat before cycling (Fig. 6a, c, and e). The surface of the graphite electrode is rough because of the micron-scale flake structure of graphite, and the silicon electrode is slightly rough compared with the $Si_{20}G_{80}$ composite electrode because of the larger size of SiCWP. After 250 cycles, the graphite electrode caused severe fragmentation and formed large cracks (Fig. 6b), which caused the current collector to disconnect from the active material. Similarly, after a long cycling process, the silicon electrode surface generated a large number of fluffy products due to the volume

expansion of silicon particles (Fig. 6d), sharply weakened electrical contact between the active material and the current collector, and thus, deteriorated its cycle performance dramatically. Damaging the electrode integrity and electric conductive pathways, electrode mud-cracking is a notorious culprit for polarization increase and capacity fading.[34] However, the surface of the $Si_{20}G_{80}$ composite electrode after cycling was more evenly distributed than that of the graphite and silicon electrodes (Fig. 6f). Although showing fragmentation, the smaller cracks had a more uniform distribution, which allowed the electrode to maintain a good contact with the current collector, so that it has a good cycle performance. To sum up, the combined graphite indeed promotes the uniform distribution of silicon in carbon, buffers the volume expansion of silicon and helps to maintain the stability of the whole electrode.

XPS C 1s and F 1s spectra of the post-cycled electrodes are shown in Fig. 6g and h, respectively. The C 1s spectra were distributed into five peaks (around 284.6 eV, 285.6 eV, 286.9 eV, 289.2 eV and 290.4 eV), corresponding to C–C, C–O, $ROCO_2Li$, Li_2CO_3 and $–CF_x$ species, respectively. The relatively strong $–CF_x$ peak indicated a high content of fluorocarbon in SEI, which is mainly due to the reduction in FEC.[35,36] It is well known that FEC has the lowest unoccupied molecular orbitals (LUMOs) in carbonate solvent molecules and is preferentially reduced to form an F-rich SEI layer with superior passivation.[37] The composition rich in F in the SEI layer promotes lithium ion transport and ensures the stability of the Si/C particle electrode interface.[38,39] However, electrode cracking can expose a large area of the inner surface of the fresh electrode, enabling the penetration and reduction of a large amount of electrolytes.[40] Given the limited dose of FEC in this study (5 wt%), electrode cleavage accelerates FEC consumption. Therefore, the larger
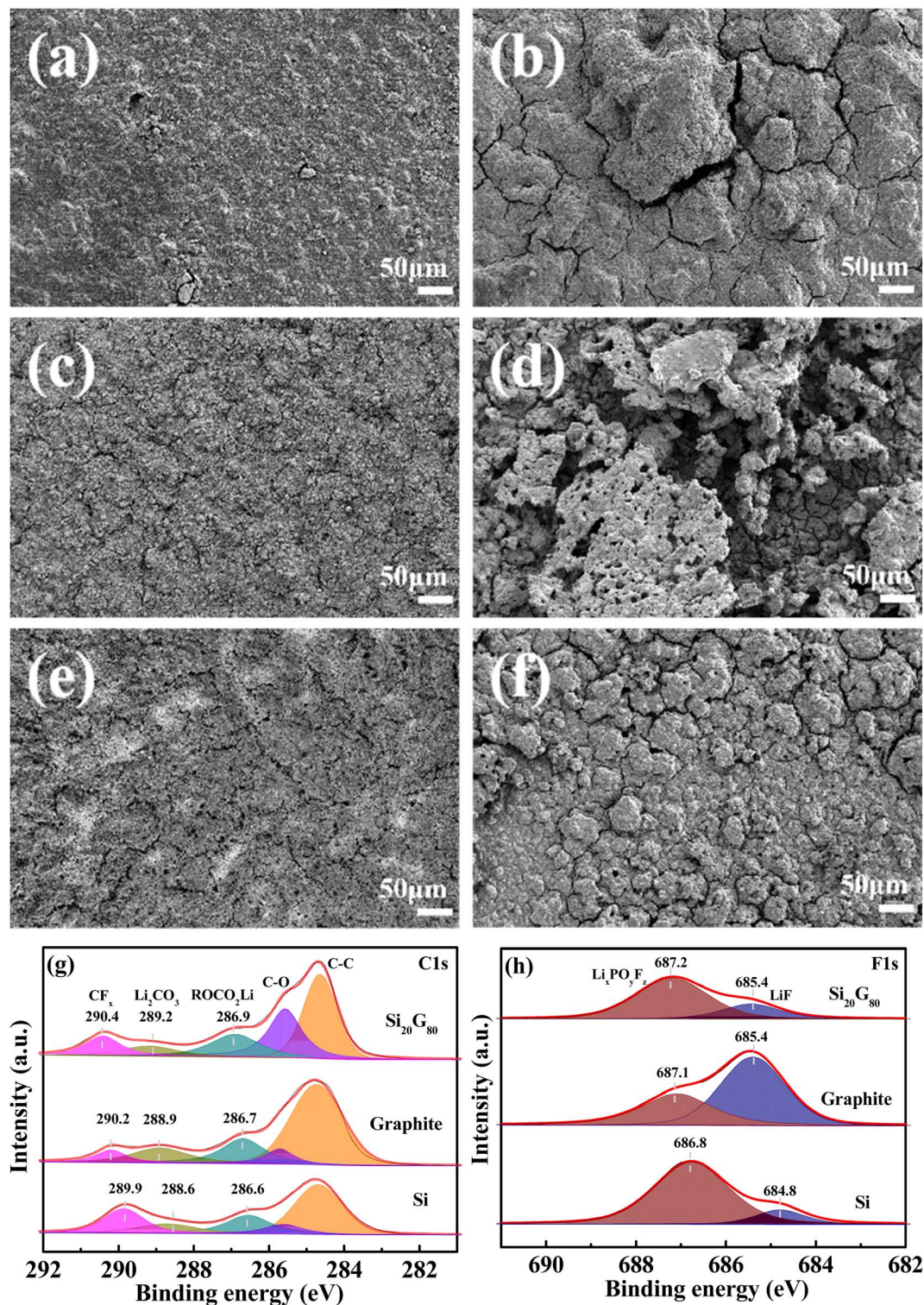
Fig. 6   SEM images of graphite, Si and $Si_{20}G_{80}$ electrodes before (a, c and e) and after 250 cycles (b, d, and f) at 1 C; XPS C 1s (g) and F 1s (h) spectra of the posted cycled electrodes.

and more the cracks, the easier the formation of SEI membranes, as can be seen from the binding energy of C 1s and F 1s. According to the binding energy of $ROCO_2Li$, Li_2CO_3, $-CF_x$, LiF and $Li_xPO_yF_z$, the trend is Si < graphite < $Si_{20}G_{80}$. Because of the crack caused by silicon volume expansion, it is easy to form

an SEI film, followed by graphite, the good surface morphology of the $Si_{20}G_{80}$ composite can protect the electrode well, and the formation of SEI film becomes more difficult, thus the binding energy increased. The comparison of the contents of fluorinated compounds from the XPS F 1s spectra of the post-cycled

Table 3   Comparison of the contents of fluorinated compounds

Sample	Peak area of LiF	Peak area of $Li_xPO_yF_z$	Total area	Conversion ratio
Graphite	158 586.9	93 916.89	252 503.79	1
Si	29 825.8	177 821.4	207 647.2	0.82
$Si_{20}G_{80}$	35 637.72	109 923.4	145 561.12	0.57

electrodes (Fig. 6h) is shown in Table 3. Thanks to the small cracks and uniform distribution, the $Si_{20}G_{80}$ composite electrode exhibits the smallest content of fluorine compounds.

According to the previous description, the price of recovery of SiCW and graphite is $690 and 4000-a-tonne, respectively. For $Si_{20}G_{80}$ the cost is $3338 per ton, plus pretreatment costs (about $100 per ton), for a total price of around $3400 per ton, which is still much lower than the current market price of silicon-based anode materials ($16 000 per ton).

4.   Conclusion

In this study, low-cost silicon cutting waste (SiCW) was used as the raw material to prepare high-purity nano-silicon particles by pretreatment and then compounded with graphite to improve the electrochemical performance of silicon anodes. Spherical Si@graphite composite nanoparticles (diameter less than 150 nm) effectively reduced the particle pulverization caused by repeated intercalation/delithiation during cycling, and the graphite coating on the silicon surface buffered the volume change of silicon and restrained the volume expansion effectively. Meanwhile, the uniform dispersion of nano-silicon in graphite carbons effectively improved the electrical conductivity of silicon, and ultimately improved the electrochemical performance of the silicon-based anode. All the results indicate that $Si_{20}G_{80}$ has excellent fast charge–discharge performance and good reversibility, which is very suitable for electric vehicles for fast charge requirements. Adopting low-cost raw materials and industrialization-based preparation processes can effectively control the production cost of silicon-based anode materials, and lay a solid foundation for their practicality.

Data availability

All data included in this study are available from the corresponding author upon request.

Conflicts of interest

There are no conflicts to declare.

Acknowledgements

References

1 Y.-K. Sun, Z. H. Chen, H.-J. Noh, D.-J. Lee, H.-G. Jung, Y. Ren, S. Wang, C. S. Yoon, S. T. Myung and K. Amine, Nanostructured High-Energy Cathode Materials for Advanced Lithium Batteries, Nat. Mater., 2012, 11, 942–947.

2 M. Armand and J.-M. Tarascon, Building Better Batteries, Nature, 2008, 451, 652–657.

3 X. Ge, S. Liu, M. Qiao, Y. Du, Y. Li, J. Bao and X. Zhou, Enabling Superior Electrochemical Properties for Highly Efficient Potassium Storage by Impregnating Ultrafine Sb Nanocrystals within Nanochannel-Containing Carbon Nanofibers, Angew. Chem., Int. Ed., 2019, 58, 14578–14583.

4 X. Li, M. Gu, S. Hu, R. Kennard, P. Yan, X. Chen, C. Wang, M. J. Sailor, J. G. Zhang and J. Liu, Mesoporous Silicon Sponge as An Anti-pulverization Structure for High-performance Lithium-ion Battery Anodes, Nat. Commun., 2014, 5, 4105.

5 Y. Fang, X. Xu, Y. Du, X. Zhu, X. Zhou and J. Bao, Novel Nitrogen-Doped Reduced Graphene Oxide-bonded Sb Nanoparticles for Improved Sodium Storage Performance, J. Mater. Chem. A, 2018, 6, 11244–11251.

6 Z. Xu, J. Yang, T. Zhang, Y. Nuli, J. Wang and S. I. Hirano, Silicon Microparticle Anodes with Self-healing Multiple Network Binder, Joule, 2018, 2, 1–12.

7 M. Li and Y. Zeng, Electrochemical Properties of Si–Co–Mn–Al-Modified Graphite Sphere Composites as Negative Electrode Materials for Li-Ion Batteries, J. Electrochem. Soc., 2010, 157(6), A729–A734.

8 Z. Xu, J. Yang, H. Li, Y. Nuli and J. Wang, Electrolytes for Advanced Lithium Ion Batteries Using Silicon-based Anodes, J. Mater. Chem. A, 2019, 7, 9432–9446.

9 D. Lin, Z. Lu, P. C. Hsu, H. R. Lee, N. Liu, J. Zhao, H. Wang, C. Liu and Y. Cui, A High Tap Density Secondary Silicon Particle Anode Fabricated by Scalable Mechanical Pressing for Lithium-ion Batteries, Energy Environ. Sci., 2015, 8, 2371–2376.

10 X. H. Liu, L. Zhong, S. Huang, S. X. Mao, T. Zhu and J. Y. Huang, Size-dependent Fracture of Silicon Nanoparticles During Lithiation, ACS Nano, 2012, 6, 1522–1531.

11 Y. Li, K. Yan, H. W. Lee, Z. Lu, N. Liu and Y. Cui, Growth of Conformal Graphene Cages on Micrometre-sized Silicon Particles as Stable Battery Anodes, Nat. Energy, 2016, 1, 1–9.

12 Y.-J. Kim, H. Yang, S.-H. Yoon, Y. Korai, I. Mochida and C.-H. Ku, Anthracite as a candidate for lithium ion battery anode, J. Power Sources, 2003, 113(1), 157–165.

13 Z. Zhang, F. Xi, S. Li, X. Wan, W. Ma, X. Chen, Z. Chen, R. Deng, J. Ji, H. J. Fan and C. Chong, High-performance Si/nano-Cu/CNTs/C Anode Derived From Photovoltaic Silicon Waste: A Potential Photovoltaic-energy Storage Strategy, Mater. Today Energy, 2021, 20(6861), 100671.

14 F. Xi, Z. Zhang, X. Wan, S. Li, W. Ma, X. Chen, R. Chen, B. Luo and L. Wang, High-performance Porous Silicon/nanosilver Anodes from Industrial Low-grade Silicon for lithium-ion batteries, ACS Appl. Mater. Interfaces, 2020, 12(43), 49080–49089.

15 M. Ko, S. Chae, J. Ma, N. Kim, H. W. Lee, Y. Cui and J. Cho, Scalable Synthesis of Silicon-nanolayer-embedded Graphite for High-energy Lithium-ion Batteries, *Nat. Energy*, 2016, **1**, 1–8.

16 X. Han, Z. Zhang, H. Chen, L. Luo, Q. Zhang, J. Chen, S. Chen and Y. Yang, Bulk Boron Doping and Surface Carbon Coating Enabling Fast-charging and Stable Si Anodes: from Thin Film to Thick Si Electrodes, *J. Mater. Chem. A*, 2021, **9**, 3628–3636.

17 Y. Tian, Y. An and J. Feng, Flexible and Freestanding Silicon/MXene Composite Papers for High-performance Lithium-ion Batteries, *ACS Appl. Mater. Interfaces*, 2019, **11**, 10004–10011.

18 X. Zhang, D. Kong, X. Li and L. Zhi, Dimensionally Designed Carbon–silicon Hybrids for Lithium Storage, *Adv. Funct. Mater.*, 2019, **29**, 1806061.

19 P. Li, G. Zhao, X. Zheng, X. Xu, C. Yao, W. Sun and S. X. Dou, Recent Progress on Silicon-based Anode Materials for Practical Lithium-ion Battery Applications, *Energy Storage Mater.*, 2018, **15**, 422–446.

20 Q. Zhou, J. Wen, J. Wu, W. Ma, K. Wei, Z. Zhang, L. Zhang and J. Xu, Recovery and Purification of Metallic Silicon from Waste Silicon Slag in Electromagnetic Induction Furnace by Slag Refining Method, *J. Clean. Prod.*, 2019, **229**, 1335–1341.

21 S. Jiang, S. Gao, J. Kong, X. Jin, D. Wei, D. Li and P. Xing, Study on the Synthesis of β-SiC Nanoparticles from Diamond-wire Silicon Cutting Waste, *RSC Adv.*, 2019, **9**, 23785–23790.

22 T. Lu, Y. Tan, J. Li and S. Shi, Remanufacturing of Silicon Powder Waste Cut by a Diamond-wire Saw through High Temperature nNon-transfer Arc Assisted Vacuum Smelting, *J. Hazard. Mater.*, 2019, **379**, 120796.

23 S. Chen, L. Shen, P.-A. Aken, J. Maier and Y. Yan, Dual-Functionalized Double Carbon Shells Coated Silicon Nanoparticles for High Performance Lithium-Ion Batteries, *Adv. Mater.*, 2017, 1605650.

24 F. Xi, Z. Zhang, Y. Hu, S. Li, W. Ma, X. Chen, X. Wan, C.-M. Chong, B. Luo and L. Wang, PSi@SiOx/Nano-Ag Composite Derived from Silicon Cutting Waste as High-performance anode Material for Li-ion Batteries, *J. Hazard. Mater.*, 2021, **414**, 125480.

25 Z. Sheng, L. Shao, J. Chen, W. Bao, F. Wang and X. Xia, Catalyst-free Synthesis of Nitrogen-Doped Graphene via thermal Annealing Graphite Oxide with Melamine and Its Excellent Electrocatalysis, *ACS Nano*, 2011, **5**, 4350–4358.

26 A. Magasinski, P. Dixon, B. Hertzberg, A. Kvit, J. Ayala and G. Yushin, High-Performance Lithium-Ion Anodes Using a Hierarchical Bottom-Up Approach, *Nat. Mater.*, 2010, **9**, 353–358.

27 J. Zhang, L. Zhang, P. Xue, L. Y. Zhang, X. L. Zhang, W. W. Hao, J. H. Tian, M. Shen and H. H. Zheng, Silicon-Nanoparticles Isolated by in situ Grown Polycrystalline Graphene Hollow Spheres for Enhanced Lithium-Ion Storage, *J. Mater. Chem. A*, 2015, **3**, 7810–7821.

28 X. Hui, R. Zhao, P. Zhang, C. Li, C. Wang and L. Yin, Low-temperature Reduction Strategy Synthesized Si/Ti$_3$C$_2$ MXene Composite Anodes for High-performance Li-ion Batteries, *Adv. Energy Mater.*, 2019, **9**, 1901065.

29 V. Augustyn, J. Come, M. A. Lowe, J. W. Kim, P. L. Taberna, S. H. Tolbert, H. D. Abruña, P. Simon and B. Dunn, High-rate Electrochemical Energy Storage through Li$^+$ Intercalation Pseudocapacitance, *Nat. Mater.*, 2013, **12**, 518–522.

30 V. Augustyn, P. Simon and B. Dunn, Pseudocapacitive Oxide Materials for High-rate Electrochemical Energy Storage, *Energy Environ. Sci.*, 2014, **7**, 1597–1614.

31 J. Wang, J. Polleux, J. Lim and B. Dunn, Pseudocapacitive Contributions to Electrochemical Energy Storage in TiO$_2$ (anatase) Nanoparticles, *J. Phys. Chem. C*, 2007, **111**(40), 14925–14931.

32 T. C. Liu, W. G. Pell, B. E. Conway and S. L. Roberson, Behavior of Molybdenum Nitrides as Materials for Electrochemical Capacitors: Comparison with Ruthenium Oxide, *J. Electrochem. Soc.*, 1998, **145**, 1882–1888.

33 J. Y. Kim, S. Jung, S. H. Kang, J. Park, M. J. Lee, D. Jin, D. O. Shin, Y. G. Lee and Y. M. Lee, Graphite–silicon Diffusion-Dependent Electrode with Short Effective Diffusion Length for High-performance All-solid-state Batteries, *Adv. Energy Mater.*, 2022, **12**(3), 2103108.

34 W. Weppner and R. A. Huggins, Determination of the Kinetic Parameters of MixedConducting Electrodes and Application to the System Li$_3$Sb, *J. Electrochem. Soc.*, 1977, **124**(10), 1569–1578.

35 J. Tan, J. Matz, P. Dong, J. Shen and M. Ye, A Growing Appreciation for the Role of LiF in the Solid Electrolyte Interphase, *Adv. Energy Mater.*, 2021, **11**(16), 2100046.

36 R. Petibon, V. L. Chevrier, C. P. Aiken, D. S. Hall, S. R. Hyatt, R. Shunmugasundaram and J. R. Dahn, Studies of the Capacity Fade Mechanisms of LiCoO$_2$/Si-Alloy: Graphite Cells, *J. Electrochem. Soc.*, 2016, **163**(7), 1146–1156.

37 W. Liu, P. Liu and D. Mitlin, Review of Emerging Concepts in SEI Analysis and Artificial SEI Membranes for Lithium, Sodium, and Potassium Metal Battery Anodes, *Adv. Energy Mater.*, 2020, **10**(43), 2002297.

38 J. Lee, M. S. Park and J. H. Kim, Stabilizing Li-Metal Host Anode with LiF-rich Solid Electrolyte Interphase, *Nano Convergence*, 2021, **8**(1), 18.

39 S. A. Han, H. Qutaish, M. S. Park, J. Moon and J. H. Kim, Strategic Approaches to the Dendritic Growth and Interfacial Reaction of Lithium Metal Anode, *Chem.–Asian J.*, 2021, **16**(24), 4010–4017.

40 H. Li, Z. Chen, Z. Kang, W. Liu and Y. Chen, High-Density Crack-Resistant Si-C Microparticles for Lithium Ion Batteries, *Energy Storage Mater.*, 2023, **56**, 40–49.